N88-21523

UNIFIED CONSTITUTIVE MODELS FOR HIGH-TEMPERATURE STRUCTURAL APPLICATIONS*

U.S. Lindholm, K.S. Chan
Southwest Research Institute
San Antonio, Texas

S.R. Bodner
Technion-Israel Institute of Technology
Haifa 32000, Israel

R.M. Weber
Pratt & Whitney
East Hartford, Connecticut 06108

K.P. Walker
Engineering Scientific Software, Inc.
Smithfield, Rhode Island 02917

Unified constitutive models are characterized by the use a single inelastic strain rate term for treating all aspects of inelastic deformation, including plasticity, creep, and stress relaxation under monotonic or cyclic loading. The structure of this class of constitutive theory pertinent for high temperature structural applications is first outlined and discussed. The effectiveness of the unified approach for representing high temperature deformation of Ni-base alloys is then evaluated by extensive comparison of experimental data and predictions of the Bodner-Partom and the Walker models. The use of the unified approach for hot section structural component analyses is demonstrated by applying the Walker model in finite element analyses of a benchmark notch problem and a turbine blade problem.

INTRODUCTION

It is well-known that accurate prediction of component fatigue lives is critically dependent on the success with which local inelastic stress/strain states in the vicinity of holes, fillets, and other strain concentration sites can be calculated. Stress/strain computations for hot section components are complicated by two factors: (1) complex component geometries, and (2) nonlinear material behavior associated with high temperature creep-plasticity effects. The latter factor is particularly significant for turbine engine components in view of the fact that the combinations of centrifugal, aerodynamic, thermal and other mechanical loads that typically occur in a flight operation are so severe that they tend to drive the underlying material response beyond accepted limits for linear elastic behavior and into the regime characterized by inelastic, time- and temperature-dependent deformation, thereby rendering elastic analysis methodologies inapplicable. Thus, an accurate account of geometrical complexities, three-dimensional and inelastic effects of hot section components requires a nonlinear finite-element methodology with an advanced material constitutive model appropriate for high temperature applications.

C. S

Advanced constitutive models which have been developed for high temperature applications are generally based on the unified approach, utilizing a single inelastic term to encompass all aspect of inelasticity, including plasticity, creep, and stress relaxation. Unified constitutive models which have been proposed in the literature include those of Walker [1], Bodner-Partom [2,3], Miller [4], Krieg, Swearengen and Rhode [5], Chaboche [6], Robinson [7], Hart [8], and Lee and Zaverl [9]. Of these newly proposed constitutive models, only a small number of them have been used in conjunction with finite-element methods for structural analysis applications. Despite the limited experience, the earlier works [1] clearly demonstrated that the unified approach is entirely compatible with three-dimensional inelastic finite-element formulations, and constitutes a new approach for structural analysis which has heretofore been based on classical concepts with uncoupled creep-plasticity models. In avoiding the simplified assumptions of classical theory, the unified theory can more realistically represent the behavior of materials under cyclic loading conditions and high temperature environments.

A joint effort by Southwest Research Institute and Pratt & Whitney Aircraft has been underway for the past two years [10,11] to: (1) develop unified constitutive models for representing high-temperature, time-dependent inelastic deformation of initially isotropic cast nickel-base alloys, and (2) apply a unified constitutive model for hot section component analysis. This effort is funded under the HOST (Hot Section Technology) Program managed by NASA Lewis Research Center. The objective of this paper is to summarize the results to date concerning the use of the unified approach for modeling high temperature deformation of nickel-base alloys and for structural analysis. In this paper, the structure of unified constitutive theories pertinent for high-temperature structural applications is first outlined and discussed. The use of the unified approach for representing high temperature deformation is then evaluated by extensive comparison of experimental data of a nickel-base alloy and predictions of two unified models: the Bodner-Partom and the Walker models. Finally, the use of the unified approach for hot section structural component analyses is demonstrated by applying the Walker model to finite element analyses of a benchmark notch problem and a turbine blade problem.

OVERVIEW OF UNIFIED CONSTITUTIVE MODELS

The "unified" models are inherently incremental (rate formulation), retaining the separation of elastic and inelastic behavior and the assumption of plastic incompressibility. Thus,

$$\dot{\varepsilon}_{ij} = \dot{\varepsilon}^e_{ij} + \dot{\varepsilon}^p_{ij} \tag{1a}$$

and

$$\dot{\varepsilon}^p_{kk} = 0. \tag{1b}$$

All inelastic behavior is represented in the single term $\dot{\varepsilon}^p_{ij}$. For small deformation, the elastic term, $\dot{\varepsilon}^e_{ij}$, follows Hooke's law. Development of the inelastic strain rate term generally includes three components: a flow law, a

kinetic relation, and a set of evolutionary equations for the internal variables describing the development of hardening and recovery processes due to deformation and thermal histories. An extensive review of the general forms for these components is given in [10,12].

Most models use the generalized form of the Prandtl-Reuss flow law, i.e.

$$\dot{\epsilon}^p_{ij} = \lambda(S_{ij} - \Omega_{ij})$$

(2)

where S_{ij} is the deviatoric stress, Ω_{ij} is also a deviatoric tensor often referred to as the equilibrium stress, back stress, or kinematic hardening variable, and λ is a scalar coefficient incorporating isotropic hardening. In one model examined (Bodner-Partom), the Ω_{ij} is dropped and directional hardening is included in an incremental scalar fashion in the coefficient λ. Eq. 2 defines the direction of inelastic flow with respect to the applied deviatoric stress S_{ij} or the effective stress $S_{ij} - \Omega_{ij}$.

The functional relationship between the scalar increments of strain rate and stress and the temperature, T, and internal variables, X_i, is called the kinetic relation, e.g.:

$$D^p_2 = F(J_2, T, X_i) ,$$

(3)

where

$$D^p_2 = \frac{1}{2} \dot{\epsilon}^p_{ij} \dot{\epsilon}^p_{ij}$$

and

$$J_2 = \frac{1}{2}(S_{ij} - \Omega_{ij})(S_{ij} - \Omega_{ij}) .$$

The number of internal variables, X_i, used is arbitrary but usually is restricted to two; one representing isotropic hardening and the other directional (kinematic) hardening. At high temperatures, the evolutionary equations for the internal variables are based on the well-accepted Bailey-Orowan theory for a hardening process proceeding with accumulating deformation and a recovery or softening process proceeding with time. The evolution rate of an internal variable is then the difference between the hardening rate and the recovery rate.

Thermal history effects are generally modeled by including thermal terms in the evolution equations for the isotropic and directional hardening variables [12,13]. The general forms of the evolution equations for the isotropic hardening variable, K, and the directional hardening variable, Ω_{ij}, are [12]:

$$\dot{K} = h_1(K)\dot{M}_1 - r_1(T,K) + \Theta_1(K,T)\dot{T}$$

(1)

373

$$\dot{\Omega}_{ij} = h_2(\Omega_{ij})\dot{M}_{ij} - d(\Omega_{ij},T)\dot{N}_{ij} - r_2(\Omega_{ij},T)V_{ij} \qquad (2)$$

$$+ \Theta_2(\Omega_{ij},T)\dot{T}\, W_{ij}$$

where h_1, r_1, and Θ_1 represent, respectively, the hardening, static thermal recovery, and thermal history functions for K; h_2, d, r_2, and Θ_2 represent the hardening, dynamic recovery, static thermal recovery, and thermal history functions for Ω_{ij}, respectively; $\dot{N}_{ij}$, V_{ij} and W_{ij} are directional indices related to unit vectors representing plastic strain rate, stress, or the directional hardening variable [12]. The measure of the hardening rate, $\dot{M}$, is taken as either the inelastic strain rate $\dot{\epsilon}^p_{ij}$ or the inelastic work rate, $\dot{W}_p = \sigma_{ij}\dot{\epsilon}^p_{ij}$.

The appropriate forms of Θ_1 and Θ_2 are not very well established at this time. A general approach for modeling thermal history effects is to express Θ_1 and Θ_2 as functions of the internal variable and temperature [12,13]. New internal variables may also be introduced [14]. In a particular approach [1,11], Θ_1 and Θ_2 are assumed to depend on temperature only and are taken as functions represented by variations of material constants with respect to temperature [1,11].

In the following sections, extensive experimental correlations with two specific models, Bodner-Partom [2,3] and Walker [1], will be presented. While following the general form outlined above, these two models differ considerably in detail but both have found considerable use in high-temperature problems. Details of both sets of equations are given in Tables 1 and 2.

EVALUATION OF THE BODNER-PARTOM AND THE WALKER MODELS

Extensive experiments were conducted on a cast turbine blade or vane alloy (PWA B1900+Hf) over the entire range of conditions experienced by hot section components, which include temperature ranging from room temperature to 1093C, strain rates from 10^{-7} to 10^{-2} sec^{-1} and strain of $\pm$ 1 percent. The B1900+Hf alloy has a grain size of .8 mm (ASTM No. -2 to -3), a γ' size of 0.9 μm in the fully heat-treated condition, and low porosity. All specimens were obtained from a single heat.

Testing included isothermal tension, creep, stress relaxation, cyclic loading (with and without mean stress or hold time), thermomechanical fatigue (TMF) cycles, and proportional and nonproportional biaxial strain cycles. Details of the experimental procedures are described elsewhere [11]. As described in [11], the material constants for the Bodner-Partom model were derived from uniaxial tension data only, while the Walker model required, in addition, a small amount of cyclic data. Tables 3 and 4 summarize the Bodner-Partom and the Walker model constants for B1900+Hf, respectively. Formalized procedures for developing model constants are being developed [11]. In the past, this function has been a major detraction from use of these models. The remaining cyclic, creep, relaxation, and biaxial data are predictions from each model.

A. Deformation Under Uniaxial Tension, Creep, and Cyclic Loading

Figure 1 shows monotonic tensile results and corresponding model calculations at three temperatures and a constant strain rate of 8.3 x 10^{-5} sec^{-1}. These monotonic stress vs strain data are used to establish the constants for the evolutionary equations of the internal variables describing hardening and recovery behavior. In the case of the Walker model, the cyclic stress-strain curves are needed, in addition, in order to differentiate between the isotropic and directional components. Similar tensile data over a wide range in temperature and strain rate are given in Figure 2. Temperature and rate variations are needed to fix the constants related to the kinetic equations. At 760 C (1400 F), hardening mechanisms are dominant, while at 1093 C (2000 F), the recovery terms in the evolutionary equations become dominant. The transition between hardening and recovery is dependent on both temperature and strain rate. At 760 C, the Walker model includes a strain-aging term which accounts for the region of negative strain-rate sensitivity.

Figure 3 shows the correlation for steady-state creep rate as a function of the applied stress at four temperatures. The hardening-recovery transition is evident in these data also. These results are predictions obtained from the monotonic tensile data.

A sample cyclic stress-strain curve at 1093 C is given in Figure 4. These are saturated (stable) loops after a small amount of cyclic hardening. Cyclic hardening or softening is included in the models. Cyclic stress-strain data obtained by incrementally increasing the strain range for completely reversed cycling (R = -1) is summarized in Figure 5 for four different temperatures. Here again, it should be emphasized that the Bodner-Partom model predictions are based on monotonic input data only.

The effects of imposed compressive and tensile mean strains on the cyclic constitutive behavior of B1900+Hf have also been investigated. The results for 760 C are summarized in Figure 6, with corresponding model predictions using both the Bodner-Partom and the Walker theories. For purposes of comparison the half stress range ($\Delta\sigma/2$), half cyclic plastic strain range ($\Delta\varepsilon_p/2$) and mean cyclic stress at both the first and sixth cycle are plotted versus the half strain range ($\Delta\varepsilon/2$) for R ratios (minimum strain/-maximum strain) of 0, -1, and -∞. Two important observations in Figure 6 are: (1) the experimental and theoretical saturated cyclic stress-strain curves ($\Delta\sigma/2$ - $\Delta\varepsilon/2$ curves) appear to be unique at a particular strain rate and temperature and are independent of the R ratio, and (2) both unified models predict a drift in the mean cyclic stress which is not always observed in the experimental data.

Stress relaxation tests were performed by holding strain at various locations of the hysteresis loops for a two minute period. Figure 7 compares model predictions and experimental results of stress relaxation during strain hold on the unloading portion of the saturated hysteresis loop of B1900+Hf at 1093 C. The Bodner-Partom calculations agree well with the experimental data for strain holds at .6% and .55%. At .5%, the experimental result indicates reverse stress relaxation as the stress is slightly increased from compression to tension during the hold period while the Bodner-Partom model predicts a

375

constant stress with essentially no stress relaxation. In principle, the reverse stress relaxation process is capable of prediction by the equilibrium stress approach. However, no stress relaxation calculations are currently available for the Walker model.

B.   Deformation Under Thermomechanical Cycling

In practice, component parts are subject to simultaneous load and thermal cycling and a dominant failure mode is thermomechanical fatigue (TMF). The ability of a unified constitutive model to predict response to TMF cycling is of prime interest and constitutes a rigorous test of the model. It is of further interest to determine whether a model based on equilibrium isothermal data can handle the nonisothermal response problem. Numerous experimental TMF cycles have been run with both in-phase and out-of-phase temperature-strain cycles and with and without hold time. Figure 8 presents a typical data vs model correlation for a simple in-phase cycle. Similar results are obtained for an out-of-phase cycle with a 60 second strain hold at maximum compressive strain, Figure 9. The cycle time for both the in-phase and out-of-phase cycles was 60 seconds. The correlation with both isothermally-based models is reasonably good, indicating that no obvious correction is needed to account for the rate of change in temperature. For materials exhibiting strong dynamic strain aging effect or microstructural changes during thermomechanical cycling, this may no longer be the case and extra terms in the constitutive model may be required.

C.   Deformation Under Biaxial Loading

Another critical test for the unified models is their ability to handle complex multiaxial stress or strain histories. Hardening laws under nonproportional loading still pose a problem in classical rate-independent plasticity. Most of these theories are based on initial yield and subsequent multiple loading surfaces with a normality rule. While unified theories can be developed based upon yield surface or plastic potential concepts [6-9], the models studied here assume viscoplastic flow occurs at all finite stress states other than $S_{ij} = \Omega_{ij}$ (Bodner-Partom assumes $\Omega_{ij} = 0$). The evolutionary equations in combination with the flow law define the incrementally-developed hardened state for each material direction.

Figure 10 shows experiment-model correlations for a strongly nonproportional strain cycle in which the axial and torsional strain are controlled to have the same effective cyclic strain amplitude with a 90° phase difference between the two inputs. This results in the nearly circular stress trajectories shown in Figure 10 along with the individual stress-strain hysteresis loops. The models, based on uniaxial data, show good qualitative agreement with some overestimate of the stress amplitudes.

Previous results with Hastelloy X [10] had shown that cyclic strain hardening under similar out-of-phase, nonproportional loading was significantly greater than that obtained under uniaxial or other proportional loading paths. For B1900+Hf, sequential proportional and nonproportional straining histories produced no differences in hardening behavior at all temperatures from 20 C to 980 C. There seems to be a difference in this

aspect of hardening between the precipitation-hardened alloys and dominantly solid solution alloys. The nonproportional strain paths also provide useful information on the correct form of the flow law. In the strain trajectories of Figure 10, there is observed a phase lag of approximately 20° between the inelastic strain rate $\dot{\epsilon}^p_{ij}$ and the deviatoric stress S_{ij}. This phase lag is reasonably predicted by the Walker model through the use of the equilibrium or back stress term, Ω_{ij}. In the Bodner-Partom approach, $\dot{\epsilon}^p_{ij}$ and S_{ij} are assumed coincident.

Figure 11 shows another more complex nonproportional path where the frequency of the shear strain is twice that of the axial strain. Again, qualitative agreement with the models is good; however, the hysteretic energy loss seems to be greater in the models than in the experiment.

HIGH TEMPERATURE STRUCTURAL ANALYSES

Preliminary effort to demonstrate the utility of the unified models for component analysis has been accomplished at Pratt & Whitney Aircraft. For this purpose, the MARC nonlinear finite element computer program was the vehicle for incorporating the viscoplastic models. The incorporation in the MARC program was achieved by means of an initial stress technique. All of the material nonlinearity in the constitutive equations is put into an initial load vector and treated as a pseudo body force in the finite element equilibrium equations. Because the models form a "stiff" system of differential equations, it is necessary to form the incremental constitutive equation appropriate to the finite element load increment by means of a subincrement technique. Then the constitutive equations are integrated over the small subincrements to form an accurate representation over the finite element load increment. The integration of the constitutive equations is currently performed by using explicit Euler forward differences with subincrement time step sizes determined by convergence and stability criteria. Other integration schemes are under investigation in the attempt to improve computational efficiency.

A. Benchmark Notch Analyses

The MARC finite-element code and the Walker model were used to analyze a number of benchmark notch problems. Elevated temperature testing of instrumented notch round specimen was also conducted to generate notch displacement data for verification of the analytical methodologies. The benchmark notch testing was conducted on specimens of design shown in Figure 12a for six load patterns at 871°C over load ranges sufficient to result in short time inelastic behavior and over load time sufficient to induce significant time-dependent inelastic notch strain. The loading conditions and the experiment procedures for the benchmark notch experiments are described in [11]. In these experiments, the radial and the diametrial displacements at the notch throat were measured.

The finite-element mech for the benchmark notch specimen is shown in Figure 12b. In one of the benchmark experiment, the notch specimen was loaded under monotonic tension at a nominal strain rate of 2×10^{-5} sec^{-1}. The variation in the diametrial displacement at the notch throat with the applied load is presented with model prediction in Figure 13. At the imposed nominal

strain rate of 2×10^{-5} sec^{-1}, the limit load was 35,800N (8050 lb). Finite element load versus displacement predictions agree well with the test data at low values of diametrial displacement, but diverge at strain conditions indicative of bulk yielding in the notch. The limit load is overestimated by 18%.

In another benchmark experiment involving dwell, the notched specimen was cycled at ± 331, ±352, ±365, ±386, and ± 414 MPa for 10 cycles at each stress level. Additionally, a minute hold was applied at both maximum tension and compression. The variation of the peak-to-peak notch displacement and the cyclic inelastic notch displacement with the cycle number is shown in Figures 14a and b, respectively. As noted in Figures 14a and b, the finite element analysis predicts the peak-to-peak variation in the throat diametrial displacement to within 14%, but underestimates the cyclic inelastic notch displacement by nearly 60% at the highest test loads. However, it should be noted that the inelastic notch displacements are quite small.

B.   Inelastic Turbine Blade Analysis

The MARC code along with the Walker constitutive model were used to analyze a turbine blade under a simulated flight loading spectrum. The FEM blade model with the temperature and engine RPM flight history are given in Figure 15. The flight history, representative of a commercial airline, has some high transient response early followed by steady cruise conditions. While thermal and mechanical response is computed continuously for the complete blade, we will present here a comparison only for a selected element between a totally elastic analysis and the viscoplastic analysis. This comparison is given in Figure 16. Besides showing the difference in response for a given problem by including viscoplastic behavior, this exercise provides some comparison of the relative computational times for the two problems. In this case, the viscoplastic computation time was about seven times as great as for the elastic case. More recent work has reduced this ratio to less than two [15].

CONCLUSIONS

Rapid advances are being made in the development of strongly nonlinear, time- and temperature-dependent constitutive models for metals used in gas turbine hot section components. These models, in conjunction with finite element structural analysis codes, will allow accurate prediction of stress histories and strain accumulation of components in service. This capability, particularly for regions of local stress concentration, is essential for reliable input into cumulative damage or crack initiation algorithms used for component life prediction. An increased coupling between constitutive models describing stable deformation states and limit conditions describing the initiation of local material instability or failure is needed.

ACKNOWLEDGEMENTS

REFERENCES

1. K. P. Walker, NASA Contract Report NASA CR 165533, 1981.

2. S. R. Bodner and Y. Partom, ASME J. of Applied Mechanics, Vol. 42, 1975, p. 385.

3. S. R. Bodner, "Evolution Equations for Anisotropic Hardening and Damage of Elastic-Viscoplastic Materials," Pro. Conference on Plasticity Today, Udine, Italy, 1983.

4. A. K. Miller, ASME J. of Eng. Mat. & Tech., Vol. 96, 1976, p. 97.

5. R. D. Krieg, J. C. Swearengen, and R. W. Rohde, in "Elastic Behavior of Pressure Vessel and Piping Components," PVP-PB-028, p. 15.

6. J. L. Chaboche, Bulletin de L'Academie des Sciences, Serie des Science Techniques, Vol. XXV, No. 1, 1977, p. 33.

7. D. N. Robinson, ORNL Report/TM-5969, 1978.

8. E. W. Hart, ASME J. of Eng. Mat. and Tech., Vol. 98, 1976, p. 193.

9. D. Lee and F. Zaverl, Jr., Acta Met., Vol. 26, No. 11, 1975, p. 385.

10. U. S. Lindholm, K. S. Chan, S. R. Bodner, R. M. Weber, K. P. Walker, and B. N. Cassenti, NASA CR-174718, May 1984.

11. U. S. Lindholm, K.S. Chan, S. R. Bodner, R. M. Weber, K. P. Walker, and B. N. Cassenti, NASA CR-174980, July 1985.

12. K. S. Chan, U. S. Lindholm, S. R. Bodner, and K. P. Walker, "A Survey of Unified Constitutive Theories," Prof. Second Symposium on Nonlinear Constitutive Relations for High Temperature Applications, NASA Lewis Research Center, Cleveland, Ohio, NASA Conf. Pub. 2369, Oct. 1984.

13. D. N. Robinson and P. A. Bartolotta, "Viscoplastic Constitutive Relationships with Dependence on Thermomechanical History," NASA Contractor Report 174836, 1985.

14. G. Cailletaud and J. L. Chaboche, "Macroscopic Description of the Microstructural Changes Induced by Varying Temperature," ICM3, Vol. 2, 1979.

15. K.S. Chan, U.S. Lindholm, S.R. Bodner, J.T. Hill, R.M. Weber, and T.G. Meyer, Third Annual Status Report, NASA Contract No. NAS 3-23925, Southwest Research Institute, 1986.

TABLE 1. SUMMARY OF BODNER-PARTOM MODEL

1. Flow Law:

$$\dot{\varepsilon}_{ij} = \dot{\varepsilon}_{ij}^e + \dot{\varepsilon}_{ij}^p$$

$$\dot{\varepsilon}_{ij}^p = \lambda S_{ij} \; ; \; \dot{\varepsilon}_{kk}^p = 0$$

with $S_{ij} = \sigma_{ij} - \frac{1}{3} \delta_{ij}\sigma_{kk}$

2. Kinetic Equation:

$$D_2^p = D_0^2 \exp \left\{ - \left[\frac{Z^2}{3J_2} \right]^n \right\}$$

with $Z = Z^I + Z^D$

$$D_2^p = \frac{1}{2} \dot{\varepsilon}_{ij}^p \dot{\varepsilon}_{ij}^p$$

$$J_2 = \frac{1}{2} S_{ij}S_{ij}$$

$$\lambda^2 = D_2^p / J_2$$

3. Evolution Equations of Internal Variables:

   a. Isotropic Hardening

$$\dot{Z}^I = m_1 \left[Z_1 + aZ_3 - Z^I \right] \dot{W}_p - A_1 Z_1 \left[\frac{Z^I - Z_2}{Z_1} \right]^{r_1}$$

where $\dot{a} = m_2(a_1 - a) \dot{W}_p \sin\theta$

   $\theta = \cos^{-1} (V_{ij}\overline{V}_{ij})$ or $\theta = \cos^{-1} (u_{ij} \overline{u}_{ij})$

   $V_{ij} = \beta_{ij}/(\beta_{kl}\beta_{kl})^{1/2}$, $\overline{V}_{ij} = \dot{\beta}_{ij}/(\dot{\beta}_{kl}\dot{\beta}_{kl})^{1/2}$

   $u_{ij} = \sigma_{ij}/(\sigma_{kl}\sigma_{kl})^{1/2}$, $\overline{u}_{ij} = \dot{\sigma}_{ij}/(\dot{\sigma}_{kl}\dot{\sigma}_{kl})^{1/2}$

   with $Z^I(o) = Z_0$; $\dot{W}_p = \sigma_{ij}\dot{\varepsilon}_{ij}^p$; $W_p(o) = 0$; $a(0) = 0$

   b. Directional Hardening

$$\dot{\beta}_{ij} = m_2 (Z_3 u_{ij} - \beta_{ij}) \dot{W}_p - A_2 Z_1 \left[\frac{(\beta_{kl}\beta_{kl})^{1/2}}{Z_1} \right]^{r_2} V_{ij}$$

   with $Z^D = \beta_{ij}u_{ij}$; $Z^D(o) = 0$, $\beta_{ij}(o) = 0$

   Material Constants: D_0, Z_0, Z_1, Z_2, Z_3, m_1, m_2, a_1

   A_1, A_2, r_1, r_2, n, and elastic constants

In most cases can set: $r_1 = r_2$, $A_1 = A_2$, $Z_0 = Z_2$

TABLE 2. SUMMARY OF THE MODIFIED WALKER THEORY (DIFFERENTIAL FORM)

$$\dot{\epsilon}_{ij}^p = \frac{\left(\frac{3}{2}S_{ij} - \Omega_{ij}\right)}{\sqrt{\frac{2}{3}\left(\frac{3}{2}S_{ij} - \Omega_{ij}\right)\left(\frac{3}{2}S_{ij} - \Omega_{ij}\right)}}\left\{\exp\left(\frac{\sqrt{\frac{2}{3}\left(\frac{3}{2}S_{ij} - \Omega_{ij}\right)\left(\frac{3}{2}S_{ij} - \Omega_{ij}\right)}}{K}\right) - 1\right\}^{1/\beta} \tag{1}$$

$$K = K_1 - K_2 e^{-\eta_7 R} - K_3 e^{-\eta_8 L} \tag{2}$$

$$\dot{L} = \left|\sqrt{\frac{2}{3}\dot{\epsilon}_{ij}^p\dot{\epsilon}_{ij}^p} - \left|\sqrt{\frac{2}{3}\dot{\epsilon}_{ij}^p\dot{\epsilon}_{ij}^p}\right|\right| \tag{3}$$

$$\dot{R} = \sqrt{\frac{2}{3}\dot{\epsilon}_{ij}^p\dot{\epsilon}_{ij}^p} \tag{4}$$

$$\Omega_{ij} = \Omega_{ijo} + \Omega_{ij1} + \Omega_{ij2} \tag{5}$$

$$\dot{\Omega}_{ij1} = \eta_2\dot{\epsilon}_{ij}^p - \Omega_{ij1}\left([\eta_3 + \eta_4 e^{-\eta_5}\log\frac{\dot{R}}{R_o}]\dot{R} + \eta_6 + \frac{1}{\eta_2}\frac{\partial\eta_2}{\partial\theta}\dot{\theta} - \frac{1}{\eta_3}\frac{\partial\eta_3}{\partial\theta}\dot{\theta}\right) + \left(\frac{\eta_2}{\eta_3} - \Omega_{ij1}\right)\frac{\partial\eta_3}{\partial\theta}\dot{\epsilon}_{ij}^p\dot{\theta} \tag{6}$$

$$\dot{\Omega}_{ij2} = \eta_{11}\dot{\epsilon}_{ij}^p - \Omega_{ij2}\left(\eta_9\dot{R} + \eta_{10} + \frac{1}{\eta_{11}}\frac{\partial\eta_{11}}{\partial\theta}\dot{\theta} - \frac{1}{\eta_9}\frac{\partial\eta_9}{\partial\theta}\dot{\theta}\right) + \left(\frac{\eta_{11}}{\eta_9} - \Omega_{ij2}\right)\frac{\partial\eta_9}{\partial\theta}\dot{\epsilon}_{ij}^p\dot{\theta} \tag{7}$$

$$\overset{o}{\Omega}_{ij} = 3\Omega\left[\frac{\dot{C}_{ik}C_{kj}}{C_{pq}C_{pq}} + \frac{C_{ik}\dot{C}_{kj}}{C_{pq}C_{pq}} - \left(\frac{2C_{ik}C_{kj}}{C_{pq}C_{pq}}\right)\left(\frac{C_{rs}\dot{C}_{rs}}{C_{uv}C_{uv}}\right)\right] + \left[3\frac{C_{ik}C_{kj}}{C_{pq}C_{pq}} - \delta_{ij}\right]\dot{\frac{\partial\Omega}{\partial\theta}} \tag{8}$$

$$S_{ij} = \sigma_{ij} - \frac{1}{3}\delta_{ij}\sigma_{kk} \tag{9}$$

Material Constants: λ, μ, $\overset{o}{\Omega}$, β, η_2, η_3, η_4, η_5, η_6, η_7, η_8, η_9, η_{10}, η_{11}, K_1, K_2, K_3, dependent on temperature, θ

TABLE 3. BODNER-PARTOM MODEL CONSTANTS FOR B1900+Hf

o Temperature-Independent Constants

m_1 = .270 MPa^{-1}
m_2 = 1.52 MPa^{-1}
q_1 = 0.0
Z_1 = 3000 MPa
Z_3 = 1150 MPa
$r_1 = r_2 = 2$
$D_0 = 1 \times 10^4$ sec^{-1}

o Temperature-Dependent Constants

Constants	Temperature, °C			
	T ≤ 760°C	871°C	982°C	1093°C
n	1.055	1.03	.850	.70
Z_0 (MPa)	2700	2400	1900	1200
$A_1 = A_2$ (sec^{-1})	0	.0055	.02	.25
$Z_2(=Z_0)$ (MPa)	2700	2400	1900	1200

o Elastic Moduli for B1900+Hf

$E = 1.987 \times 10^5 + 16.78\ T - .1034\ T^2 + 1.143 \times 10^{-5}\ T^3$ MPa with T in °C.

$G = 8.650 \times 10^4 - 17.58\ T + 2.321 \times 10^{-2}\ T^2 - 3.464 \times 10^{-5}\ T^3$ MPa with T in °C

382

TABLE 4.   CONSTANTS FOR THE EXPONENTIAL FORM OF WALKER'S MODEL FOR B1900+HF

Temp, °C	21	427	538	649	760	871	982	1093
E (Modulus), MPa	1.900 E+5	1.900 E+5	1.900 E+5	1.800 E+5	1.655 E+5	1.438 E+5	1.249 E+5	1.161 E+5
ν (Poisson's Ratio)	.322	.328	.331	.334	.339	.324	.351	.351
K_1, MPa	12.4	12.4	12.4	12.4	13.8	16.6	13.8	9.0
K_2, MPa	0	0	0	0	0	0	0	0
K_3, MPa	0	0	0	0	0	0	0	0
β, MPa	1.73 E11	1.73 E11	1.73 E11	3.862 E10	2.55 E10	5.50 E12	4.20 E10	5.5? E9
n_2, MPa	2.41 E6	2.41 E6	2.41 E6	8.27 E5	8.27 E5	2.36 E6	9.65 E4	2.36 E4
n_3	4794.	4794.	4794.	1714.	1880.	621.2	400.0	278.7
n_4	0	0	0	0	-585	0	0	0
n_5	.3117	.3117	.3117	.3117	.3117	.3117	.3117	.3117
n_6	0	0	0	0	0	8.73 E-4	4.79 E-4	4.83 E-2
n_7	0	0	0	0	0	0	0	0
n_8	0	0	0	0	0	0	0	0
n_9	11.87	11.87	11.87	16.64	19.83	59.33	136.0	136.0
n_{10}	0	0	0	0	2.44 E-3	2.44 E-3	2.44 E-3	2.44 E-3
n_{11}, MPa	4.70 E3	4.70 E3	4.70 E3	4.70 E3	4.70 E3	9.65 E2	0	0
$\dot{a}$, MPa	0	0	0	0	0	0	0	0
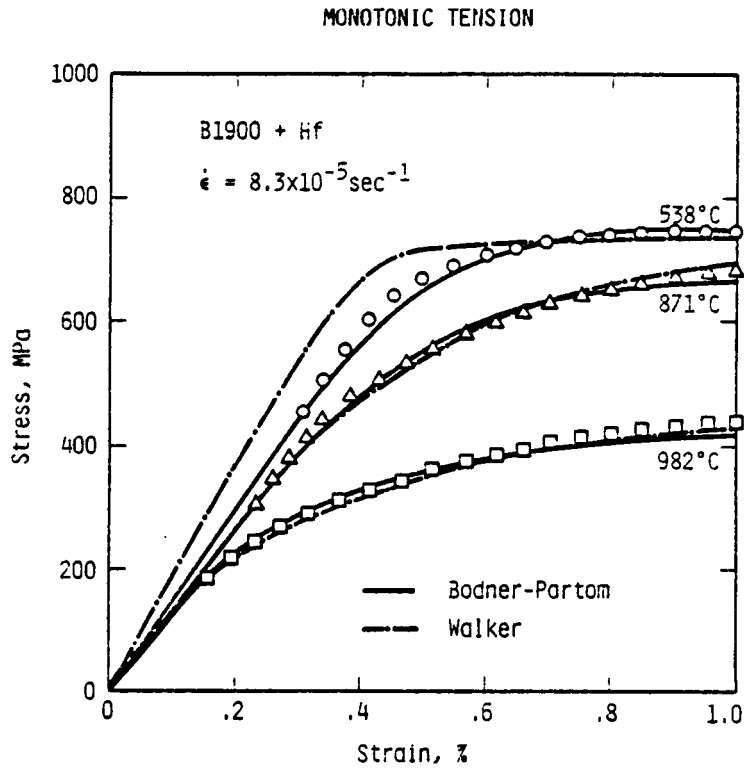
FIGURE 1.   COMPARISON OF CALCULATED AND EXPERIMENTAL
STRESS-STRAIN CURVES AT THREE TEMPERATURES
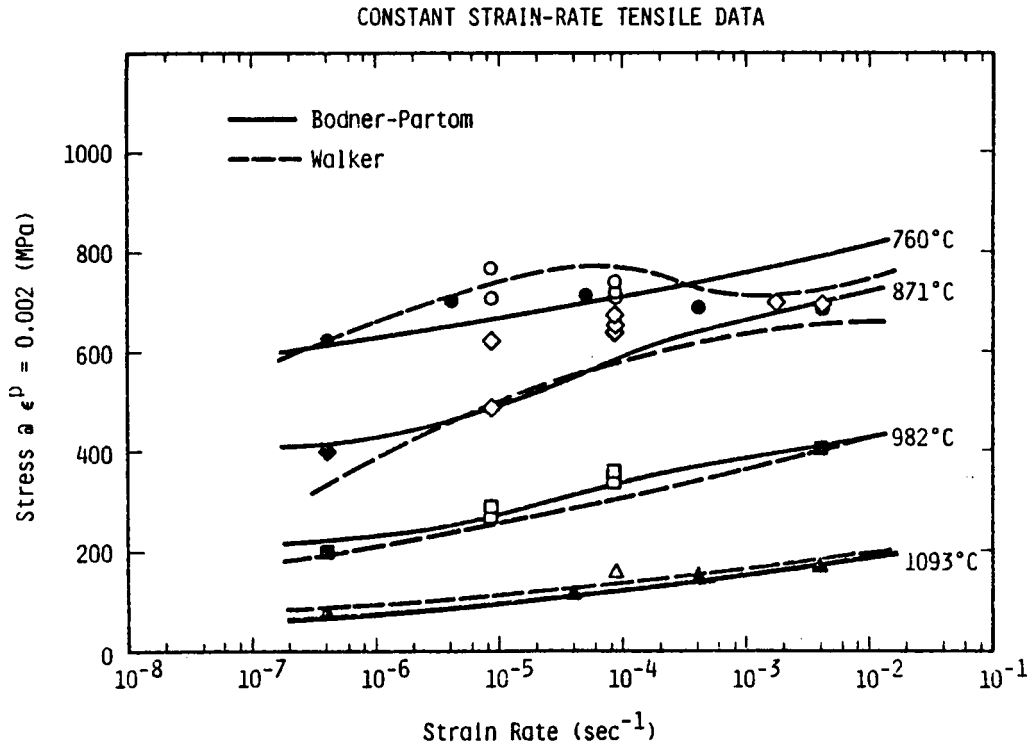
FIGURE 2.   CALCULATED AND EXPERIMENTAL RESULTS FROM CONSTANT
STRAIN-RATE TENSILE TESTS

TENSILE CREEP RATE DATA
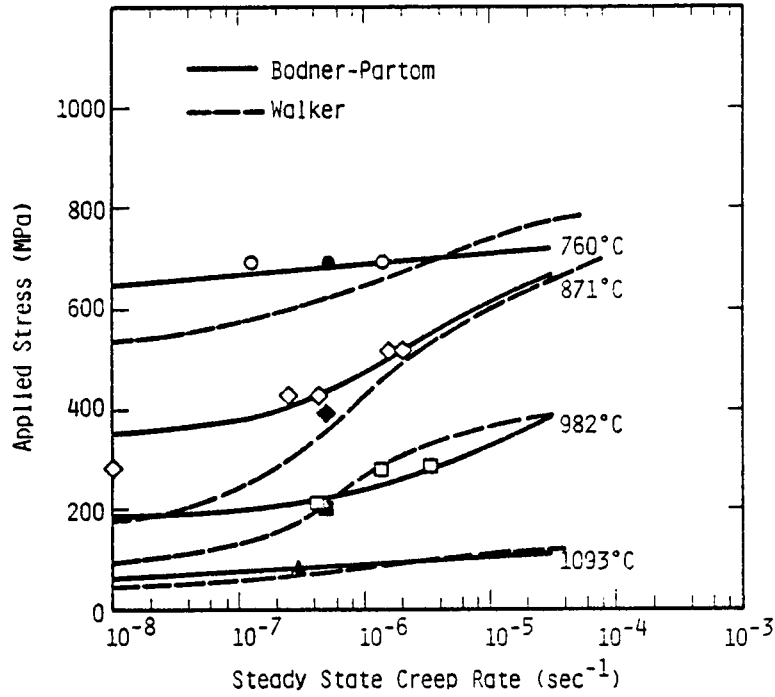
FIGURE 3. CALCULATED AND EXPERIMENTAL RESULTS
OF CONSTANT LOAD CREEP TESTS
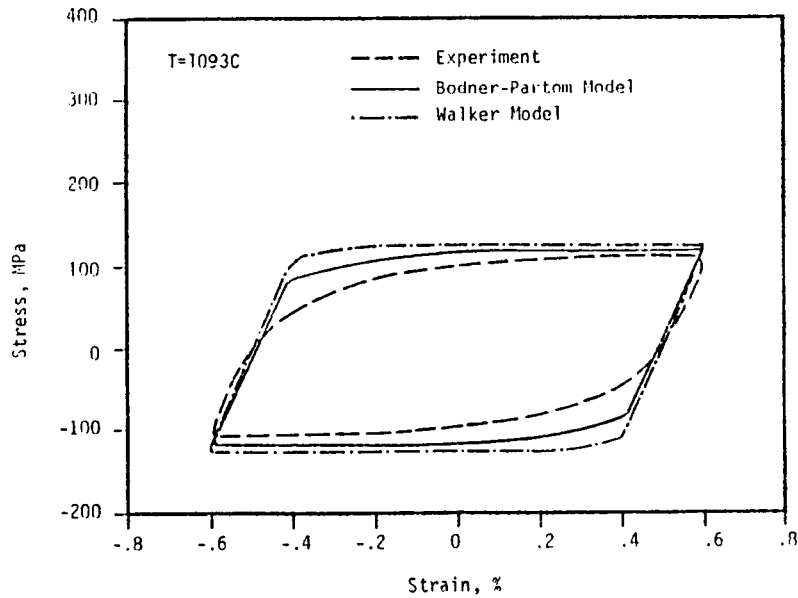
FIGURE 4. COMPARISON OF THE EXPERIMENTAL AND CALCULATED
STABLE HYSTERESIS LOOPS AT 1903 C

385
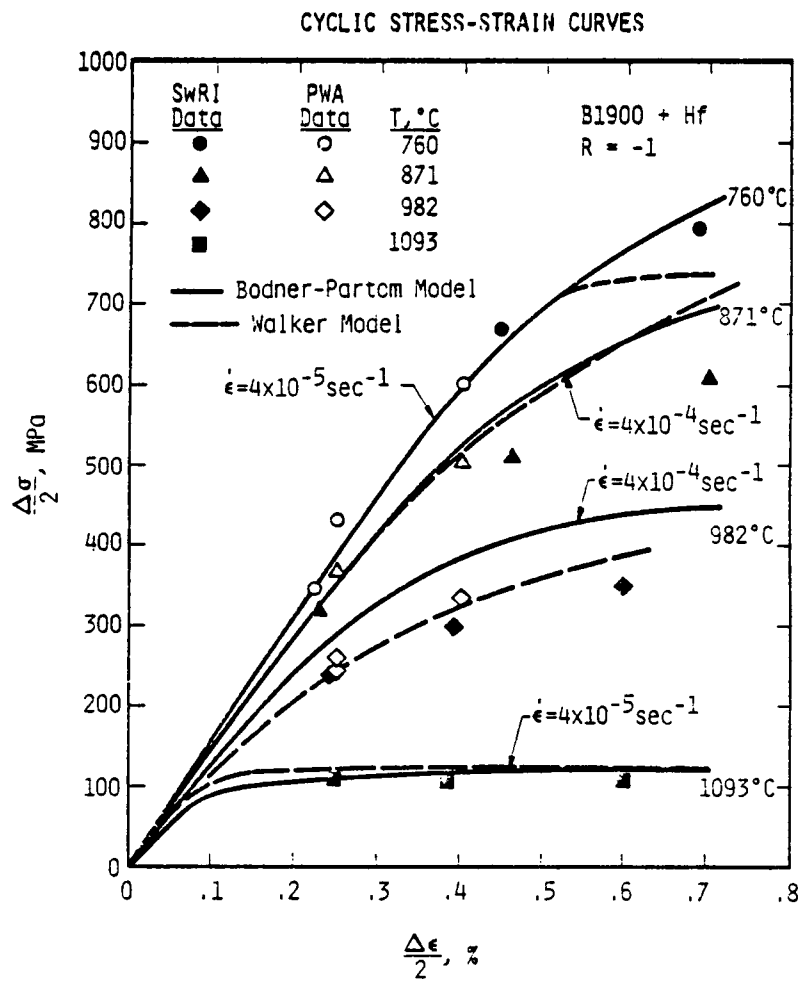
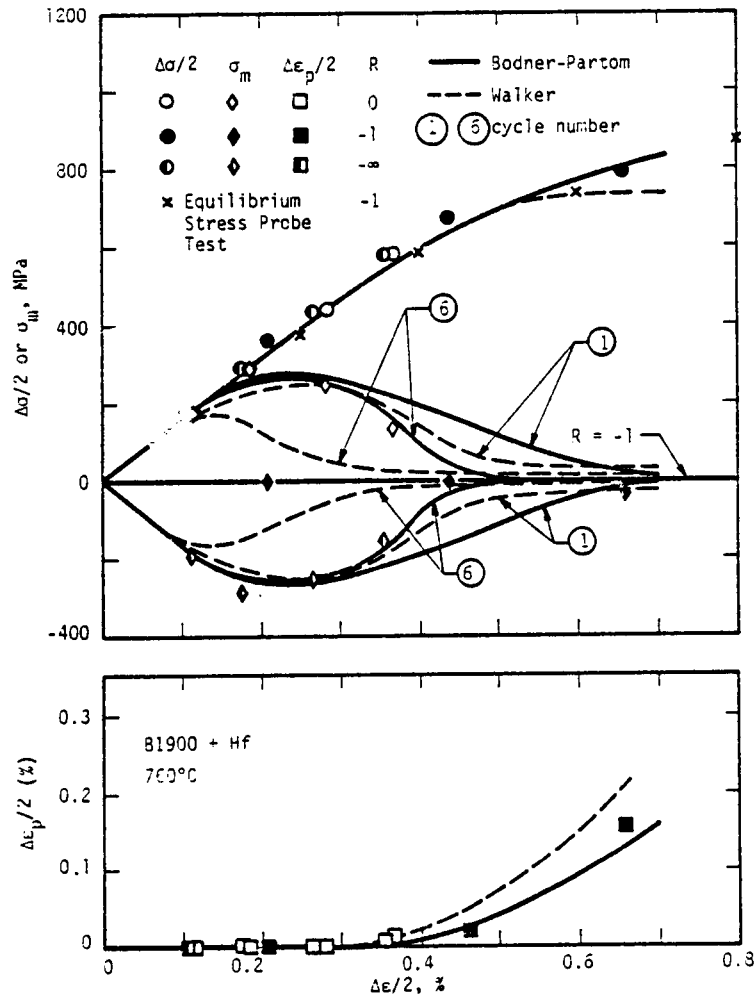FIGURE 5. CYCLIC STRESS-STRAIN CURVE AT VARIOUS TEMPERATURES

FIGURE 6. CORRELATION OF CYCLIC STRESS-STRAIN DATA WITH
MODEL PREDICTIONS AT 760°C

Stress Relaxation at Strain Hold
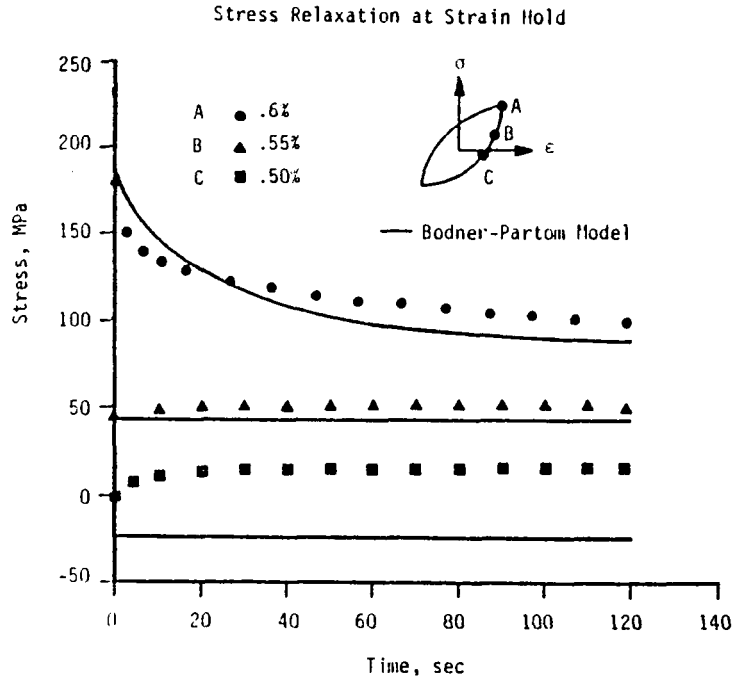
FIGURE 7.   STRESS RELAXATION DATA AT THE UNLOADING
            BRANCH OF A HYSTERESIS LOOP COMPARED
            WITH BODNER-PARTOM MODEL PREDICTION AT
            1093°C
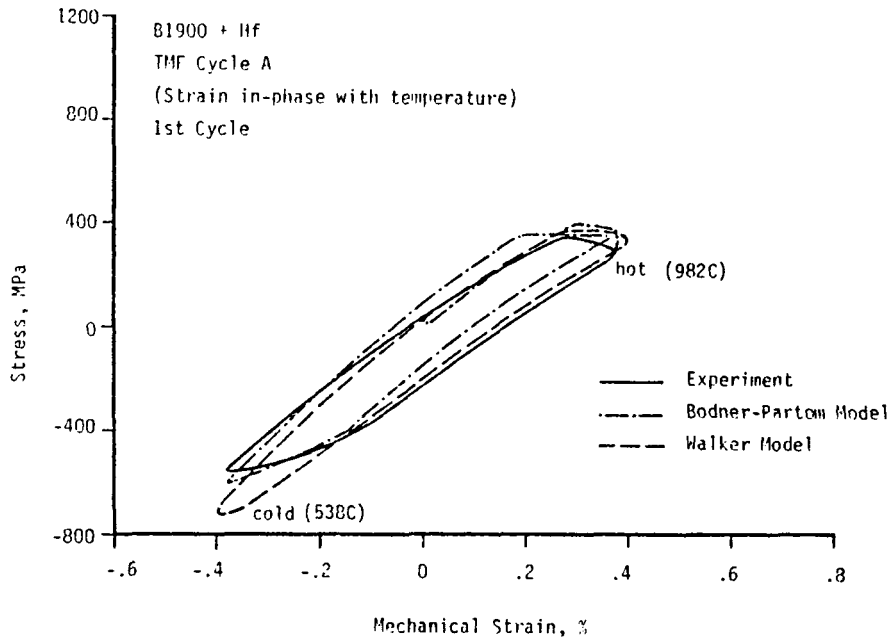
FIGURE 8.   THERMOMECHANICAL CYCLIC DATA COMPARED WITH THE WALKER
            AND THE BODNER-PARTOM MODEL PREDICTIONS FOR THE IN-
            PHASE TMF CYCLE

388

(a)

(b)
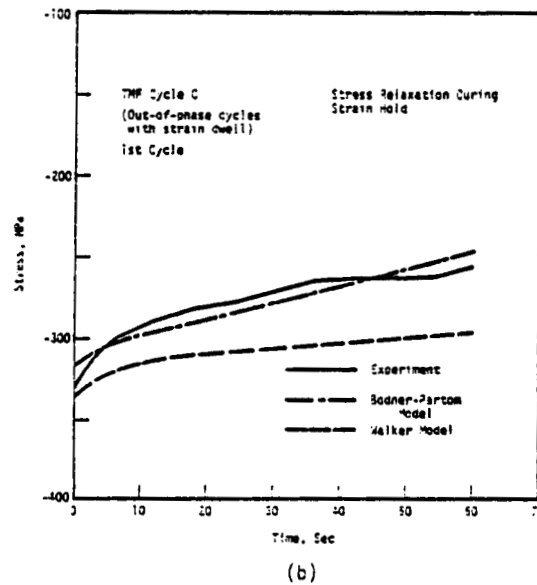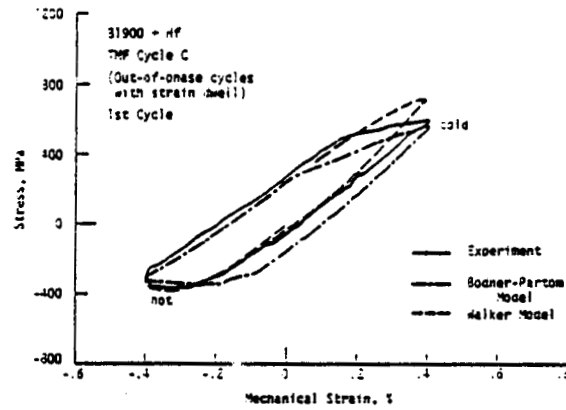
FIGURE 9. THERMOMECHANICAL DATA COMPARED WITH THE WALKER
AND THE BODNER-PARTOM MODEL PREDICTIONS FOR
THE OUT-OF-PHASE TMF CYCLE WITH STRAIN HOLD:
(A) STRESS-STRAIN RESPONSE DURING OUT-OF-PHASE
CYCLE, (B) STRESS RELAXATION RESPONSE DURING
STRAIN HOLD
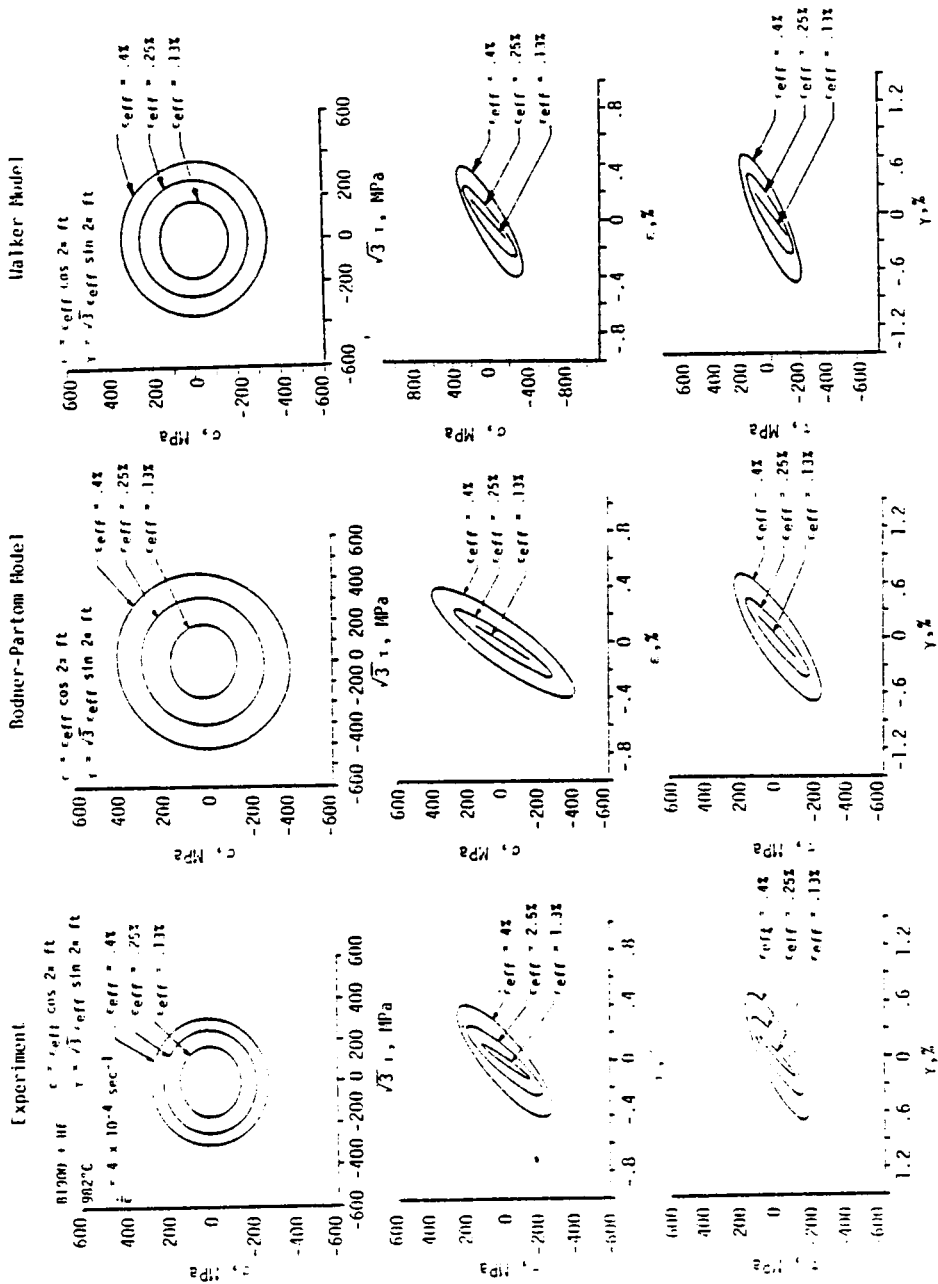
FIGURE 10. COMPARISON OF EXPERIMENTAL DATA AND MODEL CALCULATIONS SUBJECTED TO 90° OUT-OF-PHASE LOADING AT THREE EFFECTIVE STRAIN LEVELS (T = 982 C)
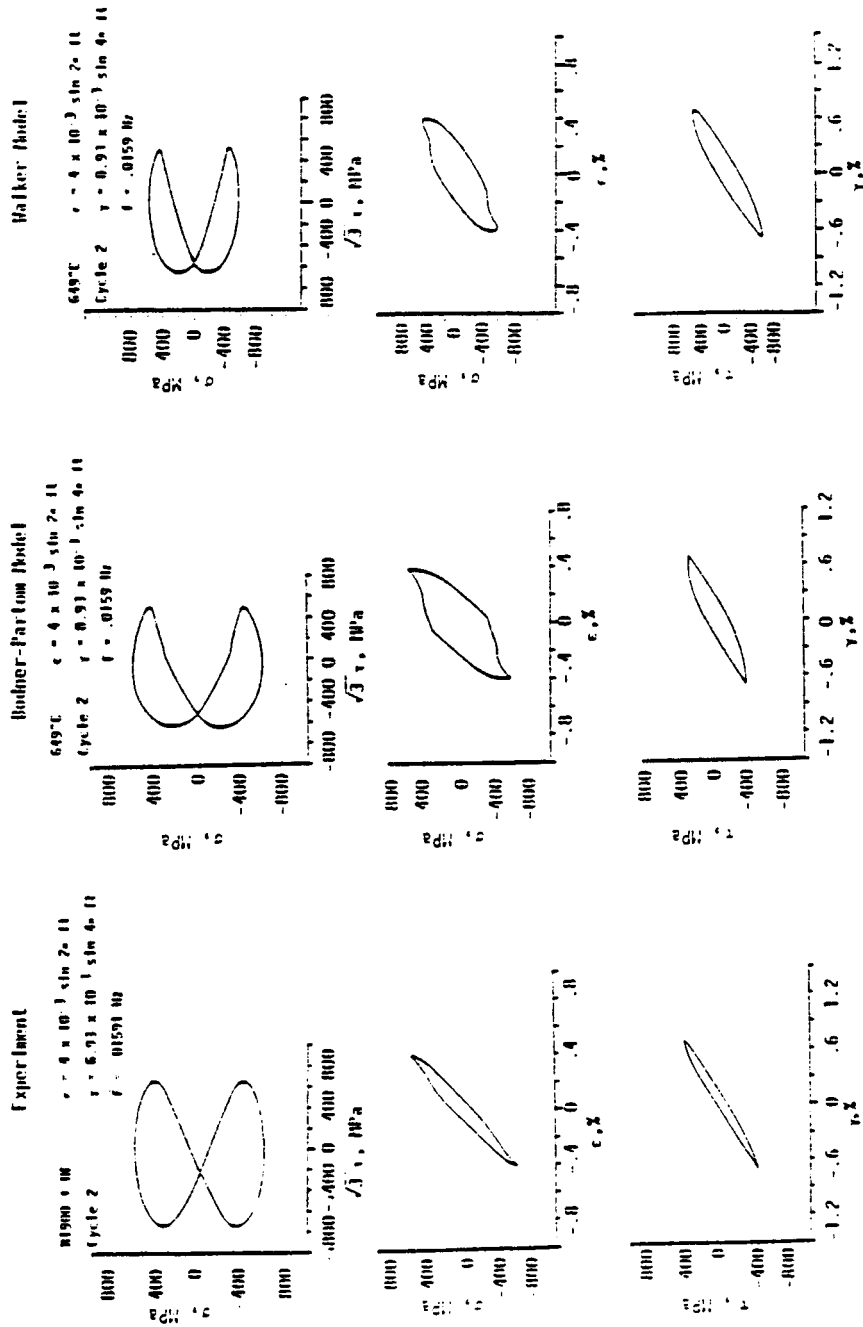
390

FIGURE 11. MODEL CALCULATIONS AND NONPROPORTIONAL MULTIAXIAL DATA WITH DOUBLE FREQUENCIES (T = 649 C)

(a)   (b)
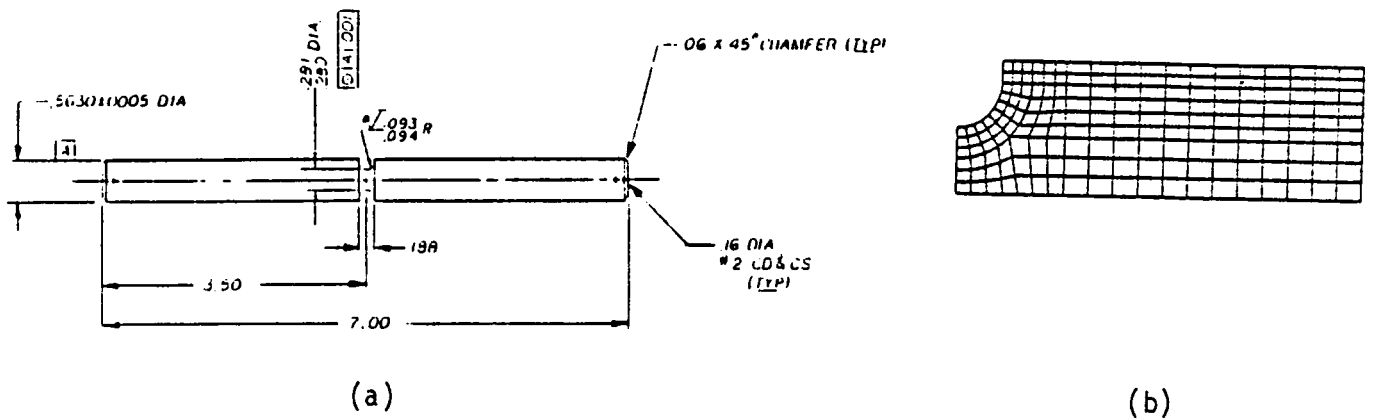
FIGURE 12.   BENCHMARK NOTCH SPECIMEN: (a) SPECIMEN
             DESIGN WITH DIMENSIONS IN INCHES, AND
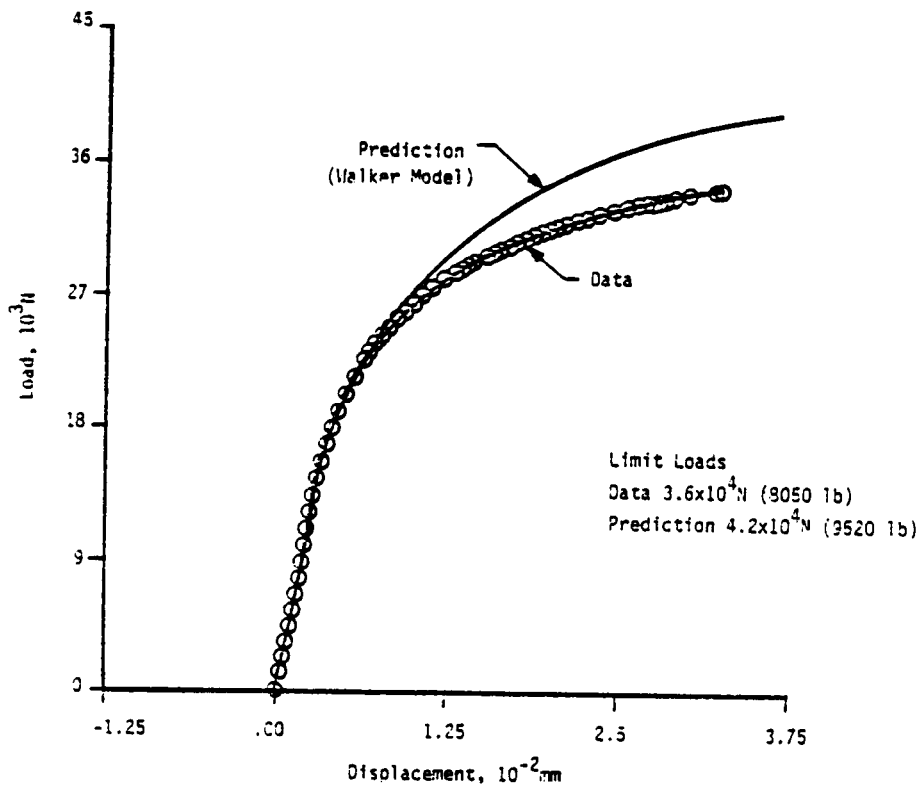   (b) FINITE-ELEMENT MECH

FIGURE 13.   COMPARISON OF EXPERIMENT AND FINITE-ELEMENT RESULT OF
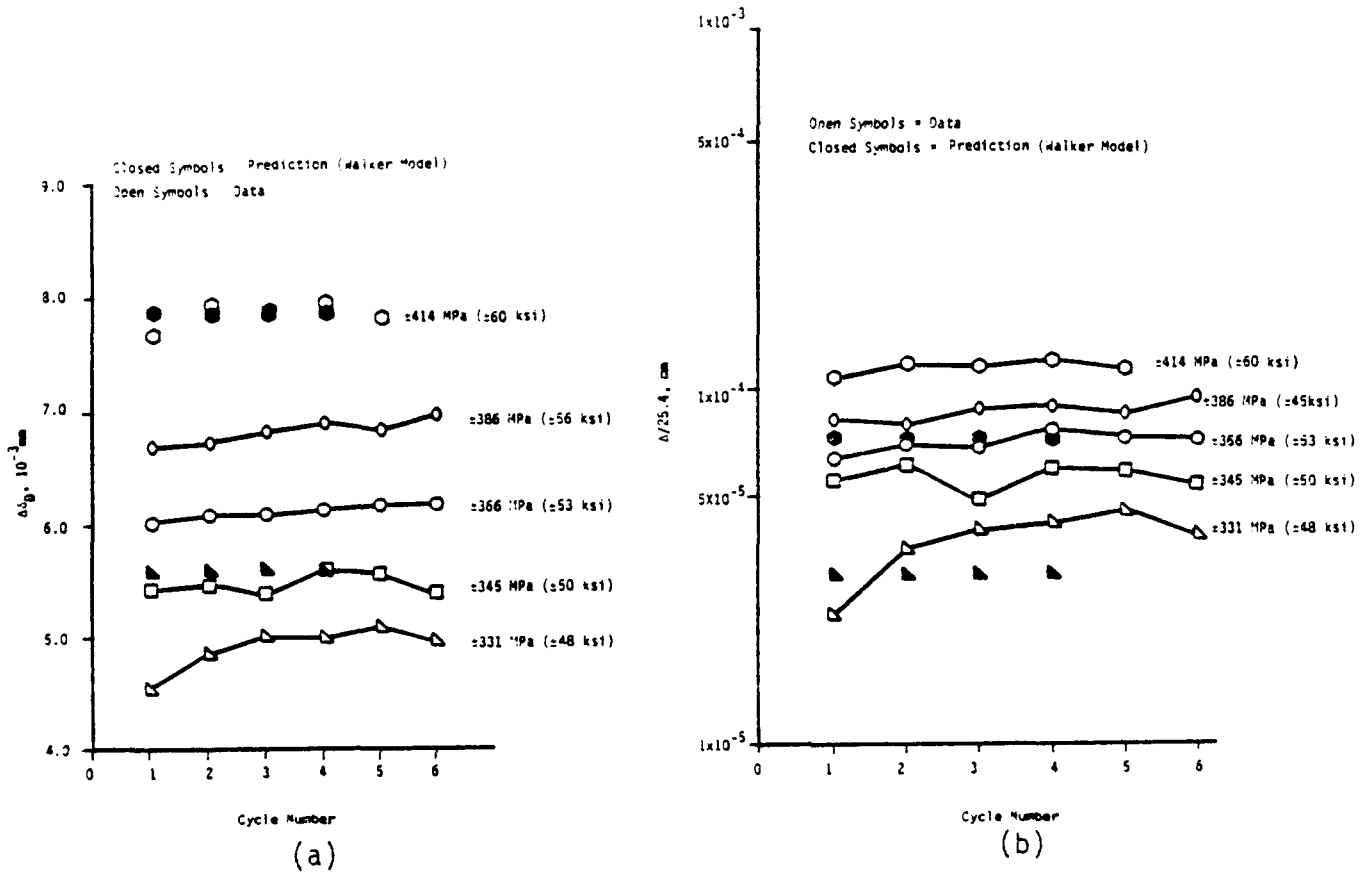   SPECIMEN UNDER MONOTONIC TENSILE LOADING

FIGURE 14. BENCHMARK NOTCH SPECIMEN UNDER FULLY REVERSED
LOADING AT 871 C WITH ONE MINUTE HOLD AT
TENSION AND COMPRESSION: (a) PEAK-TO-PEAK
NOTCH DISPLACEMENT, AND (b) CYCLIC NOTCH
INELASTIC DISPLACEMENT.

393

CONSTITUTIVE MODEL DEMONSTRATED
IN A THERMAL—MECHANICAL FLIGHT SIMULATION
OF A TURBINE BLADE

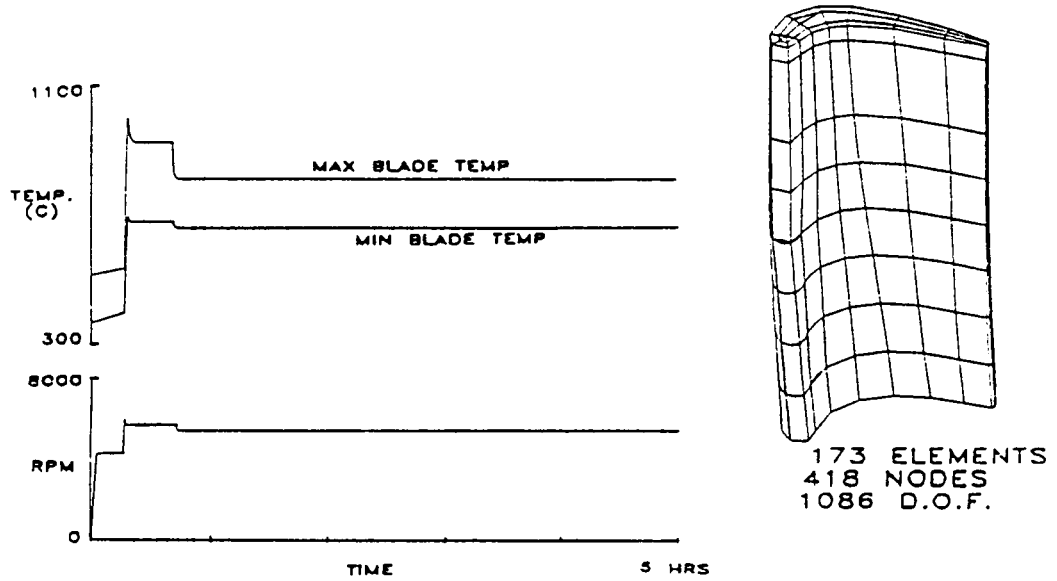173 ELEMENTS
418 NODES
1086 D.O.F.

FIGURE 15. FLIGHT SPECTRUM AND FEM BLADE MODEL USED IN A
THERMAL-MECHANICAL FLIGHT SIMULATION

ELASTIC VS INELASTIC ANALYSES
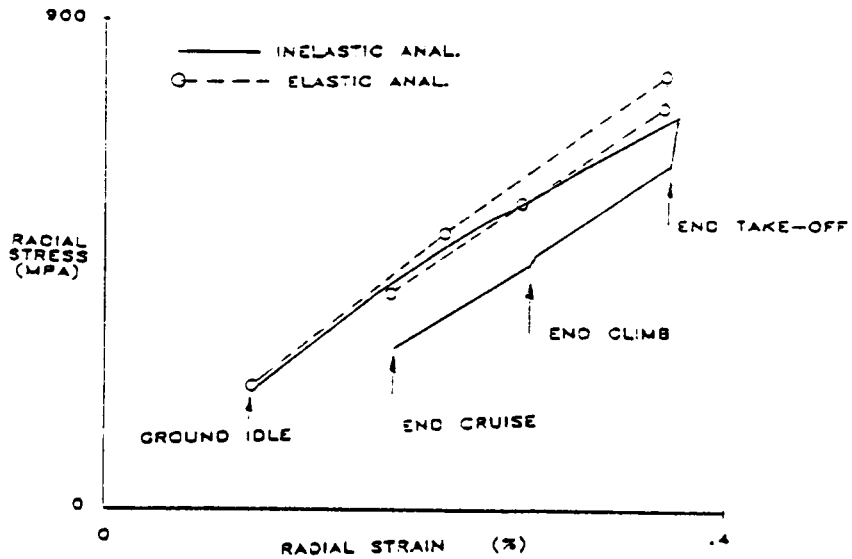
FOR A SELCTED ELEMENT

FIGURE 16. COMPARISON OF ELASTIC VS VISCOPLASTIC ANALYSIS
FOR A SELECTED BLADE ELEMENT